Journal of Rock Mechanics and Geotechnical Engineering 8 (2016) 314–328

Contents lists available at ScienceDirect

Journal of Rock Mechanics and Geotechnical Engineering

journal homepage: www.rockgeotech.org

Full length article

Design issues for compressed air energy storage in sealed underground cavities

P. Perazzelli, G. Anagnostou*

ETH Zurich, Stefano Franscini Platz 5, 8093 Zurich, Switzerland

ARTICLE INFO

Article history:
Received 2 June 2015
Received in revised form
22 September 2015
Accepted 24 September 2015
Available online 28 October 2015

Keywords:
Compressed air energy storage (CAES)
Tunnels
Lining
Concrete plug
Feasibility assessment

ABSTRACT

Compressed air energy storage (CAES) systems represent a new technology for storing very large amount of energy. A peculiarity of the systems is that gas must be stored under a high pressure ($p = 10–30$ MPa). A lined rock cavern (LRC) in the form of a tunnel or shaft can be used within this pressure range. The rock mass surrounding the opening resists the internal pressure and the lining ensures gas tightness. The present paper investigates the key aspects of technical feasibility of shallow LRC tunnels or shafts under a wide range of geotechnical conditions. Results show that the safety with respect to uplift failure of the rock mass is a necessary but not a sufficient condition for assessing feasibility. The deformation of the rock mass should also be kept sufficiently small to preserve the integrity of the lining and, especially, its tightness. If the rock is not sufficiently stiff, buckling or fatigue failure of the steel lining becomes more decisive when evaluating the feasible operating air pressure. The design of the concrete plug that seals the compressed air stored in the container is another demanding task. Numerical analyses indicate that in most cases, the stability of the rock mass under the plug loading is not a decisive factor for plug design.

1. Introduction

Very large amount of energy can be stored either with pumped hydroelectric storage (PHS) reservoirs or with compressed air energy storage (CAES) systems. PHS technology is commonly used and there are several examples in operation, while for CAES only two commercial projects have been undertaken in salt rock (Crotogino et al., 2001; Gardner and Haynes, 2007), as well as one demonstration project (Mansson and Marion, 2003) and one verification project in granite (Stille et al., 1994).

CAES systems have the peculiarity that gas must be stored under a high pressure ($p = 10–30$ MPa) in order to achieve greater efficiencies during energy recovery (withdrawal stage). Lined and unlined tunnels, shafts and caverns can all be used within this pressure range. The rock mass surrounding the opening resists the internal pressure while the lining or the natural hydraulic and geological conditions ensure gas tightness (Kovári, 1993). A lined rock cavern (LRC) is the most attractive option and the one most investigated over the past 20 years due to its wider application field, and there is no requirement for particular hydrogeological conditions or great depths of cover (Kovári, 1993).

From a geotechnical and structural point of view, the key factors to be considered in a feasibility assessment of CAES in lined cavities are: (1) uplift failure of the overlying rock up to the surface; (2) failure and loss of tightness of the sealing membrane; and (3) shearing of the plug closing the cavern. The loss of tightness of the cavity not only decreases the efficiency of the system, but also may impair stability (high air pressures within the overlying rock mass increase uplift risk). The lining concept most investigated for underground CAES is a composite structure consisting of an inner thin steel shell and an outer reinforced concrete shell (see Fig. 1). In this case, the sealing membrane is the thin steel shell. It may fail due to the bending that occurs when it is squeezed into cracks in the outer concrete lining, buckling during depressurization, the tensile stress developing during cavity expansion or the fatigue induced by cyclical loading (Damjanac et al., 2002; Okuno et al., 2009).

However, few works have analysed these aspects, and in most cases only for site-specific geotechnical conditions. Recent analyses of the uplift problem include those of Kim et al. (2012), Perazzelli et al. (2014) and Tunsakul et al. (2014). Kim et al. (2012) suggested a limit equilibrium model assuming that the full shearing resistances of the rock mass act along the vertical slip surfaces. This assumption is uncertain in view of the tensile stress field developing

* Corresponding author. Tel.: +41 (0)44 6333180.
E-mail address: georg.anagnostou@igt.baug.ethz.ch (G. Anagnostou).
Peer review under responsibility of Institute of Rock and Soil Mechanics, Chinese Academy of Sciences.

http://dx.doi.org/10.1016/j.jrmge.2015.09.006

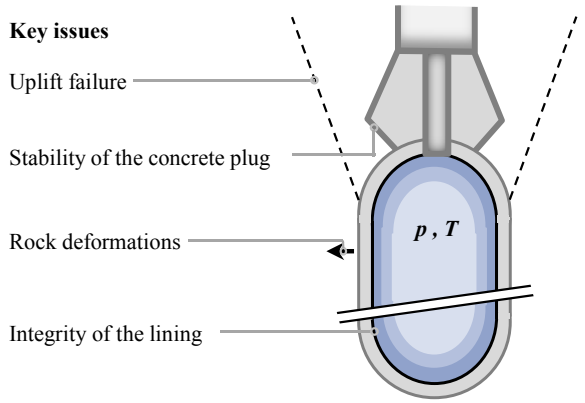

Fig. 1. Key design issues for a lined CAES rock cavity.

around the expanding cavity. Perazzelli et al. (2014) performed small and large strain numerical analyses of a continuum rock mass model and showed that the deformations at failure are very large in the case of weak rocks, thus necessitating a geometrically nonlinear formulation in order to obtain the ultimate uplift pressure. Tunsakul et al. (2014) developed a numerical method based on the element-free Galerkin (EFG) method with a cohesive crack model to simulate the fracture propagation patterns in a continuum medium around the pressurised tunnel; the authors found a qualitative agreement between physical model tests and numerical results and they emphasised that the in situ stress ratio has a strong influence on both the crack initiation location and the propagation path.

Analysis of the rock mass deformations in pressurised lined cavities can be found in Stille et al. (1994), Sofregaz US Inc. and LRC (1999), Brandshaug et al. (2001), Damjanac et al. (2002), Johansson (2003), and Okuno et al. (2009). Stille el al. (1994) and Johansson (2003) presented monitoring results from in situ tests in the Grängesberg Pilot Plant (a 9 m high shaft of 4.4 m in diameter, 50 m deep in granite). Okuno et al. (2009) presented the results of in situ tests at the Gas Storage Pilot Plant in the Kamioka mine (a 400 m deep, 6 m in diameter tunnel in sedimentary rocks). Both works showed that the cavern diameter increases with the loading cycles. Sofregaz US Inc. and LRC (1999), Brandshaug et al. (2001) and Damjanac et al. (2002) investigated the rock deformations for the Grängesberg Pilot Plant and for the Halmstad Demonstration Plant (a 50 m high cavern with 37 m in diameter, 115 m deep in granite, pressurised at 20 MPa) by numerical stress analysis of continuum rock mass models. In these studies, the rock mass is taken as a homogeneous, continuous, linearly elastic-perfectly plastic, no-tension material ($\sigma_t = 0$) obeying the Mohr–Coulomb yield criterion, and the effect of the cycling loading is not investigated. Damjanac et al. (2002) also performed numerical stress analysis of discontinuum rock mass models for the Halmstad Demonstration Plant considering the cycling loading. These analyses indicate a small increase in the magnitude of the rock mass displacements with the cycles.

Buckling and fatigue failures of the steel lining in CAES and gas storage caverns were investigated in very few works. Results of buckling analysis were presented by Okuno et al. (2009), but the computational model adopted in this work remains unclear. Verifications of fatigue can be found in Damjanac et al. (2002).

Concrete plug stability has been investigated mostly in the context of PHS systems. Auld (1983) and Ilyushin (1988) described different types of underground plugs, analysed the factors to be considered in design, and suggested a simple design formula addressing the possible failure modes in the plug, in the rock mass or at the interface – but without analysing the stability of the rock mass explicitly (the equation suggested considers the bearing capacity of the rock as an input parameter). Hökmark (1998) evaluated the stability of the rock around the concrete plug by introducing a safety factor based on an elastically computed stress field and the Mohr–Coulomb failure criterion. Park et al. (2001) performed a numerical investigation of the mechano-hydraulic behaviour of concrete plugs taking a fixed air pressure and assumed elastic behaviour for the plug concrete. They also considered the elastic-perfectly plastic behaviour according to the Mohr–Coulomb failure criterion for the rock, and elastic-perfectly plastic Mohr–Coulomb behaviour for the rock–plug interface. Their computations showed the influence of several factors (e.g. the shape, depth and in situ horizontal stress coefficient K_0) on stresses and displacements in the rock mass and the plug.

Studies on the stability of concrete plugs in CAES systems are to be found in Song and Ryu (2012) and in Pedretti et al. (2013). The approach of Song and Ryu (2012) is similar to that of Hökmark (1998). Pedretti et al. (2013) performed numerical stress analyses on the plug of a planned CAES test plant in Switzerland and evaluated the safety margin against failure by iteratively reducing the strength parameters of the rock mass.

The present paper investigates the above-mentioned design problems for underground CAES by means of numerical stress analyses, taking tunnels and shafts above the water table of 4 m in diameter with a thin steel shell under a wide range of geotechnical conditions. As in Sofregaz US Inc. and LRC (1999), Brandshaug et al. (2001) and Damjanac et al. (2002), we consider the rock mass as a homogeneous, continuous, linearly elastic-perfectly plastic, no-tension material ($\sigma_t = 0$), obeying the Mohr–Coulomb yield criterion.

We show in detail how the stress field in the surrounding rock and the displacements change during the pressurisation of a CAES cavity and we define an uplift safety criterion based on the extension of the tensile failed zone above the cavity (Section 2).

Rock mass deformations at the walls of the cavity are shown for a wide range of geotechnical conditions and a maximum operating pressure of 20 MPa (Section 3). These values are computed assuming a monotonic increasing of the air pressure. The behaviour of the adopted rock mass model in the case of loading cycles is discussed by a computational example (Section 4).

We show the stress and strain in the steel lining during pressurisation and depressurisation of the cavity and we clarify why buckling and fatigue failures can occur (Section 4). Verifications of these failures are presented (Section 4). Critical buckling loads are here computed by means of nonlinear buckling analysis, while critical stress ranges are taken from the literature.

We analyse the interaction between a site-specific rock mass and plugs of different geometries (Section 5) by means of a computational model similar to the one of Park et al. (2001). The stability of the rock around the concrete plug is investigated evaluating the relation between the pressure in the cavity and the displacement of a control point of the plug.

2. Uplift

2.1. Computational model

Uplift failure is investigated by numerical stress analyses using plane strain and axisymmetric models for the tunnels and shafts, respectively. Fig. 2 shows the computational domains and boundary conditions. The analyses were performed using the finite difference code FLAC (Itasca, 2001) under the assumption of small strains. The effect of this assumption on the assessment of the limit pressure will be discussed in Section 2.3.

The rock mass is considered to be a linearly elastic-perfectly plastic, no-tension material obeying the Mohr–Coulomb yield criterion and a non-associated flow rule with dilatancy angle equal to zero. The lining is not introduced into the numerical model because

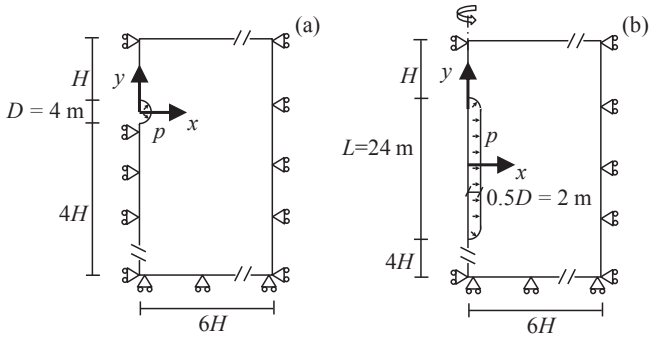

Fig. 2. Computational domains and boundary conditions for the numerical stress analyses of a CAES tunnel (a) and of a CAES shaft (b).

its stiffness is negligible compared with that of the surrounding rock; the pressurisation of the cavern causes cracking in the concrete lining and yielding of the steel shell.

The analysis consists of the following steps: (1) initialization of the in situ effective stress with a lithostatic stress distribution; (2) deactivation of the grid elements inside the tunnel or shaft and application of the average initial effective pressure; and (3) monotonic increase in air pressure up to the value at which an equilibrated solution cannot be found. The effect of the cyclical loading is not taken into account. Table 1 contains the values of the model parameters.

2.2. Failure zones and stress fields

In order to illustrate how the stress field in the surrounding rock changes during pressurisation of a cavity, we consider the example of a 50 m deep tunnel of 4 m in diameter. Fig. 3a, b and c shows the extent and type of failure of the rock mass around the tunnel for an air pressure p of 7 MPa, 17 MPa and 39 MPa, respectively. Fig. 4a, b and c shows the corresponding distributions of the radial and tangential stresses along the vertical y-axis. Of particular interest is the development of the tangential (horizontal) stress. The radial (vertical) stress obviously increases during the pressurisation of the cavity.

At a relatively low air pressure p of 7 MPa, the tangential stress drops to zero close to the tunnel and close to the surface (Fig. 4a), which means that the rock fails in tension (Fig. 3a). The tensile failure close to the surface is practically irrelevant, because the initial horizontal stress close to the surface is very low, which means that even an extremely small extensive strain would cause cracking.

With increasing air pressure, the boundary of the cracked zone around the tunnel moves radially away from the tunnel, while the cracked zone at the surface becomes deeper. When the air pressure reaches the uniaxial compressive strength of the rock, shear failure occurs at the tunnel boundary. Subsequently, a so-called *crushed zone* of increasing size develops around the cavity.

At an air pressure p of 17 MPa, the two cracked zones join together, while the crushed zone extends up to a distance of almost

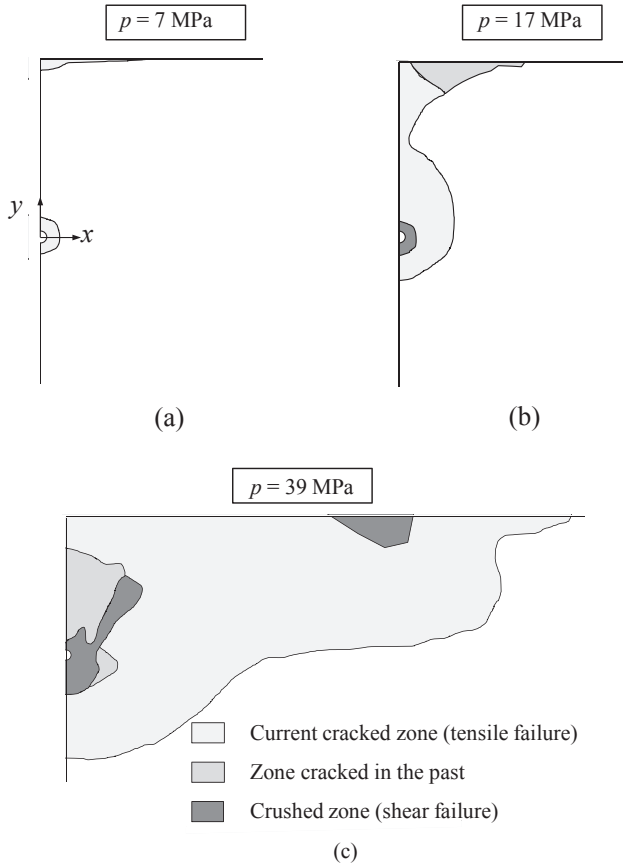

Fig. 3. Plastic zones at air pressure $p = 7$ MPa, 17 MPa and 39 MPa (tunnel of diameter $D = 4$ m, above the water table, $\gamma = 25$ kN/m^3, $\phi = 30°$, $\sigma_c = 8$ MPa, $\sigma_t = 0$, $\psi = 0°$ and $K_0 = 1$).

$D/2$ from the tunnel wall (Fig. 3b). Inside the crushed zone, the horizontal stresses are non-zero along the vertical axis of the model (they are related to the vertical stresses according to the failure criterion). Above the crushed zone, however, the horizontal stresses are zero and this continues up to the surface (Fig. 4b), indicating conceptually the presence of continuous cracks throughout the entire overburden.

At an air pressure p of 39 MPa, which is the load found at the last equilibrated solution, two separated crushed zones are observed: one extending from the tunnel to a shallow depth and another at the surface. The cracked zones are large. It is not possible to recognise the geometry of the failure mechanism.

As can be seen in Fig. 3b and c, the rock has experienced cracking in some zones in the past, i.e. at lower internal pressures. Under the current pressure, the rock in these zones is subjected only to compressive stresses. This becomes evident by comparing the distribution of the horizontal stress σ_{xx} in Fig. 4b and c. When the internal pressure increases from 17 MPa to 39 MPa, the horizontal

Table 1
Parameter values assumed in the numerical stress analysis of uplift and rock mass deformations.

Rock mass	Uniaxial compressive strength, σ_c (MPa)	Friction angle, ϕ (°)	Tensile strength, σ_t (MPa)	Dilatancy angle, ψ (°)	Young's modulus, E (GPa)	Poisson's ratio, ν
	5–60	30–40	0	0	10	0.3
Initial stress field (lithostatic)	Coefficient of lateral stress, K_0	Unit weigh, γ (kN/m^3)	Water table below the cavity			
	0.5; 1	25				

Note: The texts '0.5; 1' represent $K_0 = 0.5$ and $K_0 = 1$.

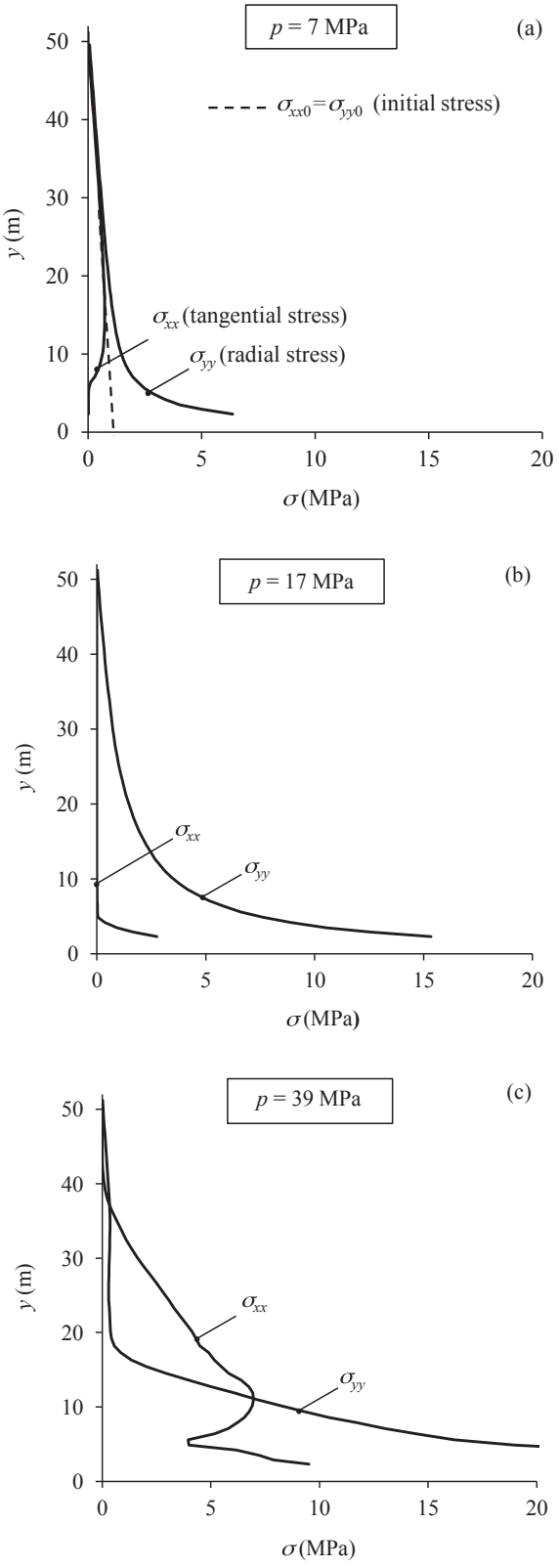

Fig. 4. Distribution of radial and tangential stresses along the vertical y-axis at $p = 7$ MPa, 17 MPa and 39 MPa (tunnel of diameter $D = 4$ m, above the water table, $\gamma = 25$ kN/m^3, $\phi = 30°$, $\sigma_c = 8$ MPa, $\sigma_t = 0$, $\psi = 0°$ and $K_0 = 1$).

stress σ_{xx} remains equal to zero only in the vicinity of the surface. When the model exhibits such behaviour, the computed deformations represent a rough approximation because the adopted elastoplastic constitutive relationships do not consider the stress-free closing of open cracks. However, such behaviour will not occur (or is limited to a small part of the model close to the surface) as long as the cracked zone does not reach the surface.

2.3. Safety criterion

A common way to investigate stability by numerical stress analyses is to evaluate the relationship between the displacement of a control point in the tunnel and the applied pressure. The instability manifests itself as an asymptotic increase in the displacement to infinity as the pressure approaches the limit value. Fig. 5 shows the relationship between the internal pressure p and the crown displacement u for the example introduced in the previous section. According to the above-mentioned failure criterion, the ultimate pressure p_{ul} is equal to 39 MPa (i.e. the pressure of the last equilibrated solution). It is important to note that the deformations at failure are very large and necessitate a geometrically nonlinear formulation. The small strain approach adopted for computing Fig. 5 overestimates the uplift pressure (Perazzelli et al., 2014).

A more conservative and intuitively reasonable criterion for safety against uplift can be derived from the extent of the cracked zone around the tunnel. As discussed previously, at a certain pressure p_c, which is lower than the ultimate pressure p_{ul}, the entire zone between tunnel and surface becomes cracked (Fig. 3b). Even if the bearing capacity of the rock mass is not fully exploited at this point, it would be sensible to avoid such a situation. To determine the critical pressure p_c, we observe the development of the cracked zone and the distribution of the horizontal stress along the vertical axis with increasing internal pressure. In the previous example, the critical pressure p_c is equal to 17 MPa (Figs. 3b and 4b). The deformations at this strain are small (<<20%), which means that the small strain formulation is adequate. Consequently, the determination of the critical pressure p_c, contrary to that of the ultimate pressure, avoids the problem of geometric nonlinearity. This provides an additional reason for evaluating safety against uplift failure from the critical pressure p_c, while incorporating an

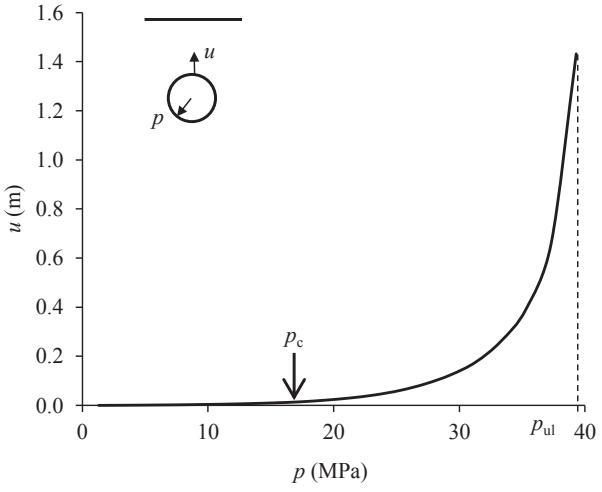

Fig. 5. Vertical displacement as a function of pressure (parameters are the same as those in Fig. 3 and Table 1).

adequate safety factor. The parametric study in the next section is based upon this criterion.

2.4. Parametric study

Figs. 6 and 7 show the critical pressure p_c for a 4 m diameter tunnel and for a 4 m diameter shaft, respectively, as a function of the overburden H for different uniaxial compressive strengths of the rock mass and in situ horizontal stresses.

The critical pressure increases almost linearly with the overburden and nonlinearly with the uniaxial compressive strength (Figs. 6b and 7b). The rock strength σ_c is important only up to a certain value, which depends on the overburden (Figs. 6b and 7b); for higher rock strengths, it is the tensile failure of the rock mass that governs the critical pressure p_c. As expected, the critical pressure increases with the in situ horizontal stress. Finally, a comparison between Figs. 6 and 7 shows that a shaft is far more favourable than a tunnel, as an overburden of 60–120 m is necessary for ensuring safety against uplift in the case of a 4 m diameter CAES tunnel, while for a CAES shaft of the same diameter, a smaller overburden of 30–50 m would be sufficient.

3. Rock mass deformations

3.1. Introduction

Sufficient safety of the rock mass with respect to uplift failure is a necessary but not a sufficient condition for the feasibility of a lined CAES cavity. The deformations in the rock mass also have to be sufficiently small to preserve the integrity of the lining and, particularly, its tightness. The present section analyses the problem of tensile failure of the steel membrane due to excessive elongation during the first pressurisation of the CAES system (cyclical loading is not considered). We assume a limit tangential deformation of the steel lining $\varepsilon_{tt,s\ lim}$ of 2%.

The computational models are the same as those used for the uplift analysis and, for the reasons explained in Section 2.1, they do not consider the contribution of lining stiffness to the overall stiffness of the system. In addition, they do not consider the cavity excavation stage. The tangential strain in the steel is taken equal to the tangential deformation of the rock mass at the boundary of the cavity, assuming that the excavation-induced rock deformations are negligible. This simplifying assumption is reasonable, because the CAES tunnels and shafts under consideration are located at relatively shallow depths and, consequently, the response of the

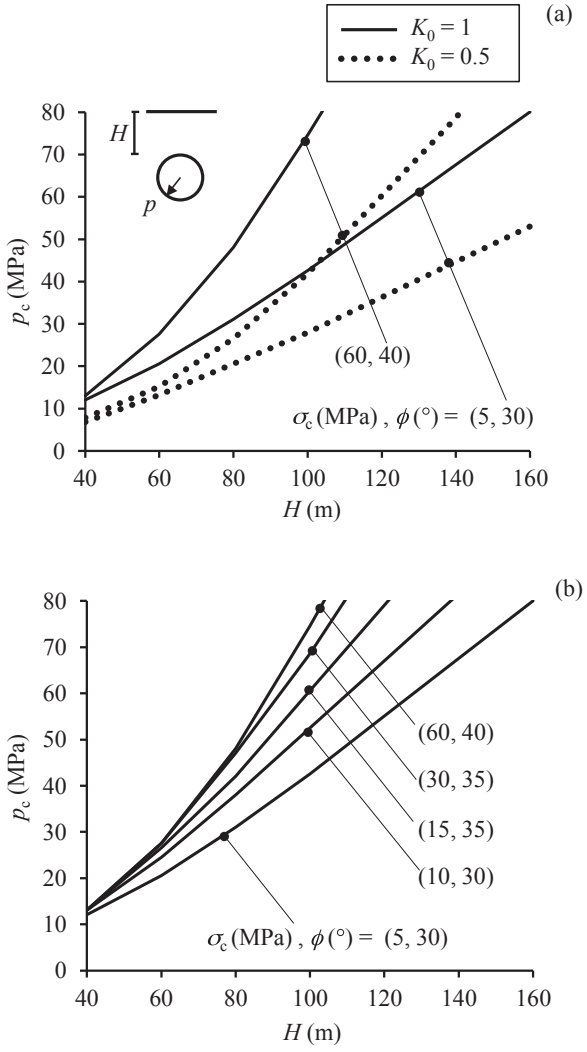

Fig. 6. Pressure p_c at which the cracked zone reaches the surface as a function of the overburden H for a CAES tunnel under different assumptions as to (a) horizontal stress and (b) rock mass strength (parameters: see Table 1).

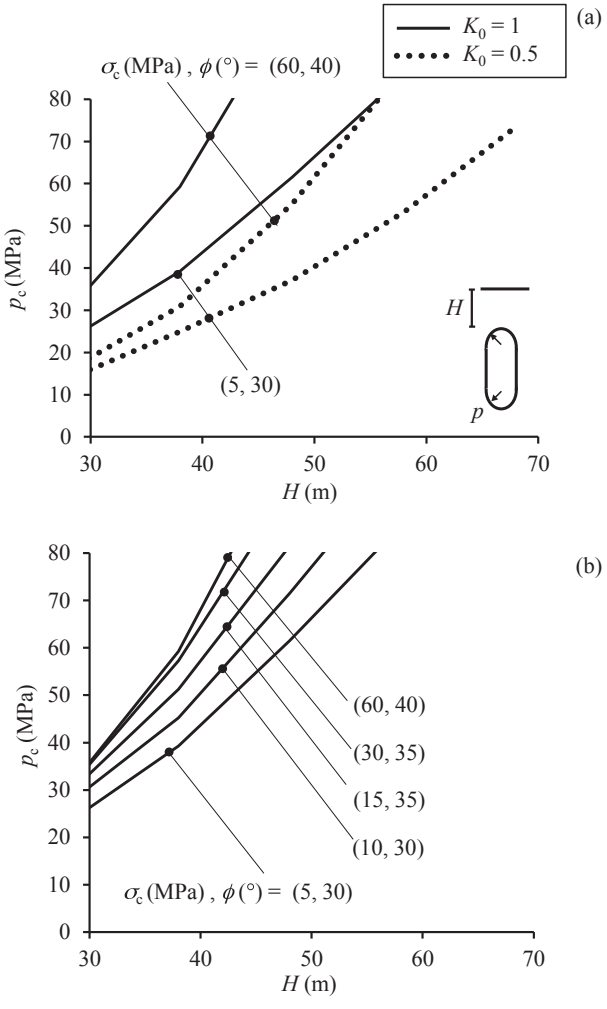

Fig. 7. Pressure p_c at which the cracked zone reaches the surface as a function of the overburden H for a CAES shaft under different assumptions about (a) horizontal stress and (b) rock mass strength (parameters: see Table 1).

surrounding rock mass to their excavation will be practically elastic.

On account of the small tangential strain limit of the steel lining ($\varepsilon_{tt,s\ lim} = 2\%$), the geometrical nonlinearity is negligible and rock deformations ε_{tt} are inversely proportional to the Young's modulus of the rock mass. For this reason, all of the analyses were performed for a specific value of the Young's modulus ($E = 10$ GPa) and their results are presented herein in terms of the product $\varepsilon_{tt}E$; the deformations for other values of the Young's modulus can be obtained by simple transformations.

3.2. Parametric study

Fig. 8 shows the maximum tangential strain ε_{tt} of the rock at the tunnel wall (multiplied by the Young's modulus E) as a function of the overburden H for a maximum operating air pressure p of 20 MPa. According to Fig. 6, uplift is not a problem for this air pressure with an overburden $H > 80$ m and the geotechnical conditions considered in Fig. 8. Depending on the strength of the rock mass and on the coefficient of lateral stress, the maximum tangential strain ε_{tt} occurs either at the tunnel crown or at the side walls (points A and B, respectively, in the inset of Fig. 8). As expected, the tangential strain ε_{tt} decreases nonlinearly with increasing rock strength σ_c, but remains constant for rock strengths higher than the air pressure of 20 MPa (shear failure does not occur in this case). Furthermore, the tangential strain ε_{tt} decreases with increasing overburden H and increasing coefficient of lateral stress K_0 (the solid lines in Fig. 8 are lower than the dotted lines). These two parameters have a major effect only in the case of a weak rock mass ($\sigma_c = 5$ MPa).

The results of Fig. 8 can be applied to determine the maximum tangential strain ε_{tt} for a given Young's modulus E. For example, if $H = 80$ m, $K_0 = 1$, $\sigma_c = 5$ MPa and $E = 500\sigma_c = 2.5$ GPa, then the maximum tangential strain $\varepsilon_{tt} = 15\%$ GPa/2.5 GPa = 6%. For a given Young's modulus E and a given limit value of the tangential strain $\varepsilon_{tt,\ lim}$ (here $\varepsilon_{tt,\ lim} = \varepsilon_{tt,s\ lim} = 2\%$), the value of $\varepsilon_{tt}E$ will be fixed and can be compared with the curves in Fig. 8 in order to assess the risk of failure of the steel lining under different geotechnical conditions. For the same rock mass considered before ($\sigma_c = 5$ MPa, $E = 2.5$ GPa), the limit value $\varepsilon_{tt,\ lim}E = 5\%$ GPa, which is lower than the curves for $\sigma_c = 5$ MPa. This indicates that CAES under a maximum air pressure of 20 MPa is not feasible in 4 m diameter lined tunnels in soft rock masses ($\sigma_c \leq 5$ MPa, $E = 500\sigma_c$) at the relatively shallow depths considered ($H < 160$ m), due to excessive deformations in the steel. On the other hand, in a higher quality rock mass with, e.g. $\sigma_c = 20$ MPa and $E = 500\sigma_c = 10$ GPa, the limit value $\varepsilon_{tt,\ lim}E = 20\%$ GPa, which is higher than the curves for $\sigma_c = 20$ MPa, thus indicating that failure of the steel due to excessive strain is not critical in this case.

Fig. 9 presents (in a similar way to Fig. 8) the results for CAES shafts of 4 m in diameter. Overburdens within the range considered will be non-critical with respect to uplift at the maximum operating pressure of 20 MPa. The maximum tangential strain ε_{tt} always occurs at the mid-height of the shaft (i.e. at $y = 0$ in the reference system of Fig. 2b). For the reasons mentioned above, the uniaxial compressive strength does not play a role if it is higher than the maximum air pressure. The effect of overburden H and coefficient of lateral stress K_0 is very small. According to the results of Fig. 9, CAES under a maximum air pressure of 20 MPa is not feasible in 4 m diameter, relatively shallow ($H < 70$ m) shafts if the rock mass is weak ($\sigma_c \leq 5$ MPa, $E = 500\sigma_c$). The deformations do not present a problem, however, in rock masses of medium-good quality ($\sigma_c \geq 20$ MPa, $E = 500\sigma_c$).

Finally, Fig. 10 shows the critical pressure p_c against uplift as well as the air pressure under which the tangential steel strain reaches the assumed limit value of 2% as a function of the overburden H for tunnels and shafts (solid and dashed lines, respectively) in a weak rock mass (the other parameters are given in the caption of Fig. 10). Safety against uplift failure is critical only for very shallow CAES tunnels ($H < 50$ m). For CAES tunnels at greater depths and for shafts (independently of the depth), deformations represent the critical factor and the overburden has only a minor effect. There is no significant difference between shafts and tunnels with respect to deformation. The reason is that the maximum tangential strain in CAES shafts occurs at their mid-height, where there are no three-dimensional effects (the horizontal shaft cross-section is like a tunnel of diameter $B = 4$ m and overburden $H+0.5L$).

4. Buckling and fatigue failures of the steel lining

4.1. Introduction

In CAES cavities, the air pressure varies cyclically between a minimum operating pressure higher than zero and a maximum pressure of 10–30 MPa. The cavity is completely depressurised during maintenance work. As explained in Section 4.3, buckling failure after the total depressurisation of the cavity and fatigue failure due to cyclical loading are important hazard scenarios even if the CAES cavity is above the water table. They are investigated in the present section by considering a 10 mm thick steel lining and

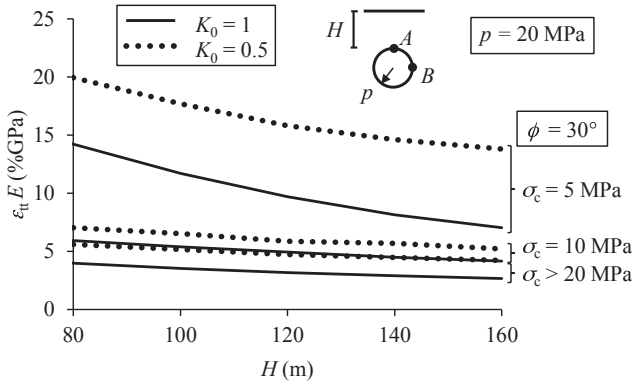

Fig. 8. Maximum tangential strain at the cavity boundary ε_{tt} multiplied by the Young's modulus E as a function of the overburden H for a CAES tunnel under an air pressure p of 20 MPa (parameters: see Table 1).

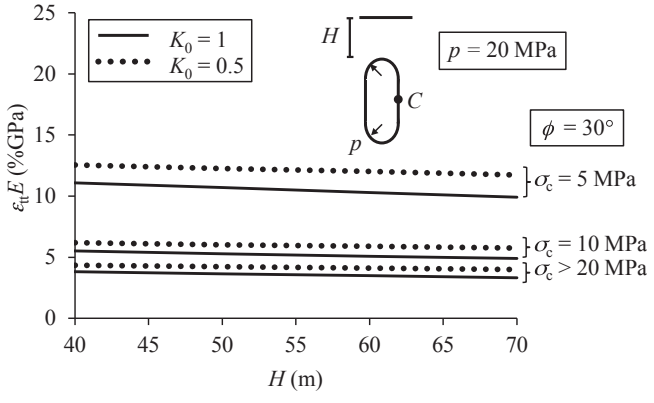

Fig. 9. Maximum tangential deformation at the cavity boundary ε_{tt} multiplied by the Young's modulus E as a function of the overburden H for a CAES shaft at air pressure $p = 20$ MPa (parameters: see Table 1).

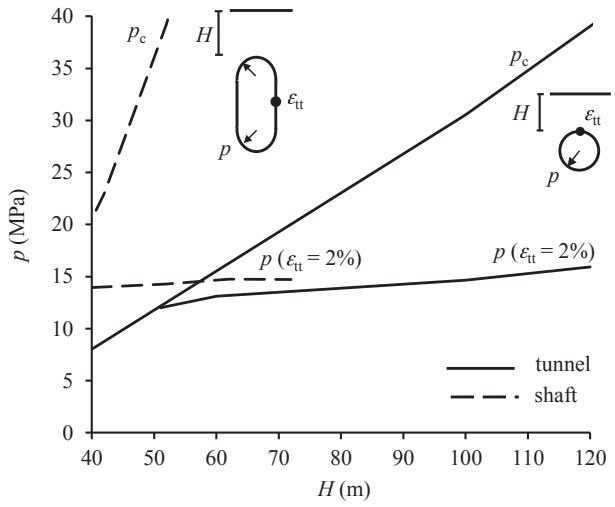

Fig. 10. Pressure p_c at which the cracked zone reaches the surface and pressure corresponding to a fixed tangential strain as a function of overburden H for a CAES tunnel (solid lines) and a CAES shaft (dashed lines) ($\phi = 30°$, $\sigma_c = 5$ MPa, $E = 2.5$ GPa, $K_0 = 1$, other parameters as in Table 1).

4 m diameter tunnels and shafts located above the water table in rock masses with an isotropic initial stress field ($K_0 = 1$). Buckling failure due to the external water pressure, which is relevant for depressurised CAES cavities beneath the water table, is not investigated here; as the steel lining is very thin, the development of water pressure must anyway be avoided (e.g. by means of a suitable drainage system).

The rock-lining interaction under cyclical loading will be analysed by means of the simple computational model, which is presented in Section 4.2. In order to better understand the interaction problem and to show certain limitations of the constitutive law of the rock mass, we discuss firstly (Section 4.3) the rock behaviour around an unlined cavity, taking two cases that concern the uniaxial compressive strength of the rock mass (rock behaviour varies depending on whether its strength is higher or lower than the maximum air pressure). Section 4.4 deals with the actual lining-rock interaction problem along with the possible failure modes of the steel lining. Finally, Sections 4.5 and 4.6 assess safety against buckling and fatigue, respectively.

4.2. Computational model

We consider a plane strain, axisymmetric model of a vertical tunnel cross-section (or a horizontal shaft cross-section). Fig. 11c shows the computational domain and the assumed boundary conditions.

The rock mass is taken as an elastic-perfectly plastic, no-tension material obeying the Mohr–Coulomb failure criterion with a non-associated flow rule (zero dilatancy angle). This constitutive model has been applied in the past to analyse monotonic cavity expansion in brittle materials (Ladanyi, 1967; Satapathy and Bless, 1995). It will be used here only for a preliminary evaluation of the above-mentioned hazard scenarios and to illustrate some potentially important limitations of this model for the cyclical loading problem.

For simplicity, we neglect the presence of tunnel support (e.g. a reinforced shotcrete layer between the steel lining and the rock) and consider the steel lining as being in direct contact with the rock mass. The steel lining is modelled as elastic-perfectly plastic and with a tensile strength equal to the yield strength of the steel. Yielding in compression is neglected because it is not expected to occur under pre-buckling loading.

The cyclical variation in the air pressure is considered to be static (dynamic effects are not taken into account). All computations assume an initial stress σ_0 of 2.5 MPa, which applies to tunnels approximately 100 m deep (or to shafts with $H + 0.5L = 100$ m). Table 2 shows the values assumed for the model parameters. The numerical analyses were performed with the finite difference code FLAC (Itasca, 2001).

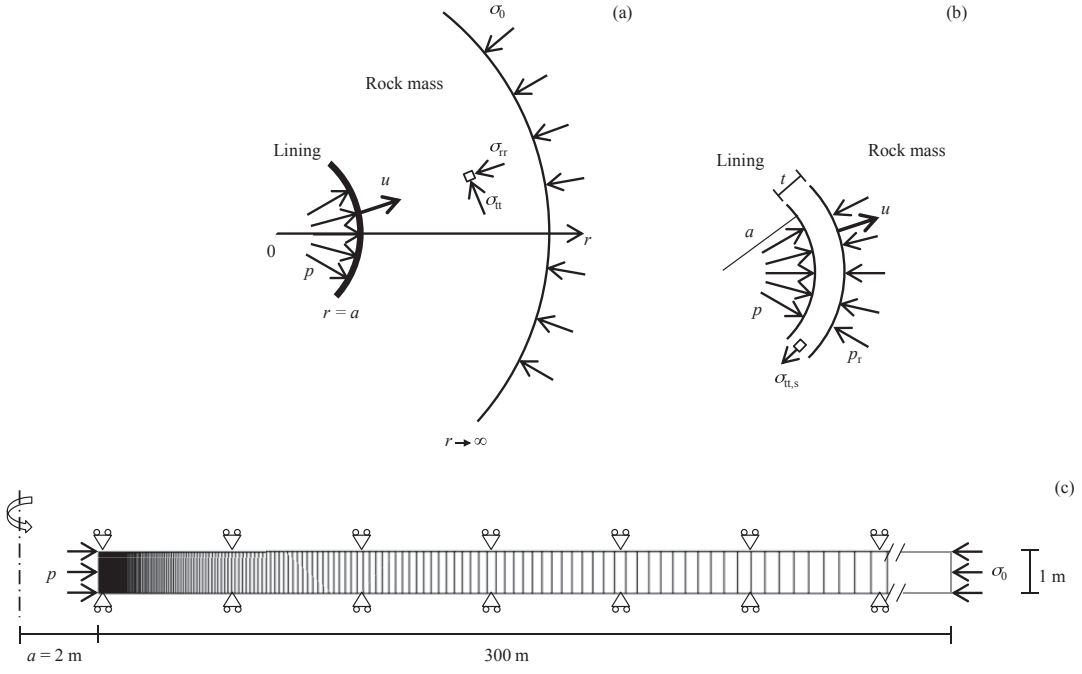

Fig. 11. Computational model adopted for the analysis of the rock-lining interaction.

4.3. Unlined cavity under cyclical loading

Behaviour under cyclical loading (air pressure variation of 0–20 MPa) will be discussed using computational results for a 100 m deep CAES tunnel (initial stress $\sigma_0 = 2.5$ MPa). Two cases will be considered: in the first case (Fig. 12), the uniaxial compressive strength, σ_c, of the rock mass is higher than the maximum air pressure ($\sigma_c > 20$ MPa). In the second case (Fig. 13), σ_c is taken equal to 7 MPa, i.e. it is lower than the maximum air pressure, which means that a crushed zone develops around the cavity as the air pressure increases above 7 MPa. In both cases, the response of the ground to the cavity excavation is elastic because the rock strength is twice greater than the initial stress.

Fig. 12a shows the stress path of a point at the cavity wall in the first case, i.e. for $\sigma_c > 20$ MPa. Point *O* shows the initial stress state; whilst path *OA* is the excavation-induced stress change. Subsequently, the radial stress at the excavation boundary is always equal to the air pressure p. During the first pressurisation of the cavity, the tangential stress decreases until it becomes equal to zero (path *AB*). This occurs at an air pressure p of $2\sigma_0 = 5$ MPa. Up to point *B*, the response of the ground is elastic and the displacement of the cavity boundary (Fig. 12c) depends linearly on the air pressure. At point *B*, the rock fails in tension. During the further pressurisation from 5 MPa to 20 MPa, the tangential stress at the cavity boundary remains equal to zero (path *BC*), while a cracked zone with an increasing outer radius develops, with the consequence that the displacement of the cavity wall increases super-linearly with air pressure (Fig. 12c). The solid lines in Fig. 12b show the radial distribution of the stresses at the maximum air pressure. The cracked zone clearly extends up to a radius of 8 m at this state.

The ground response following depressurisation is elastic. The tangential stress at the cavity wall increases by the same amount as the air pressure decreases (path *CD* in Fig. 12a) and the displacement of the cavity wall decreases linearly with decreasing air pressure. At the end of depressurisation, the tangential stress at the cavity wall is equal to the maximum air pressure (point *D* in Fig. 12a). The end of the first cycle is characterised by a residual positive displacement, i.e. by an increase in the cavity radius (Fig. 12c). The dashed lines in Fig. 12b show the radial distribution of the stresses after complete depressurisation. The stress state is clearly within the elastic domain everywhere around the cavity.

When the cavity is pressurised and depressurised again, the stress state at the cavity boundary moves along paths *CD* and *DC* (Fig. 12a), respectively; the cavity wall displacement increases and decreases linearly with the air pressure (along path *CD* in Fig. 12c); and the radial distribution of the stresses around the cavity fluctuates between the dashed and solid lines of Fig. 12b. Note that the extent of the cracked zone at the maximum air pressure does not increase with the number of cycles.

According to the computational results, the cracks that develop during the first pressurisation close during the first depressurisation and they remain closed during the following cycles. The reason for this behaviour is that the constitutive model does not account for stress-free closing of the open cracks. This can be seen clearly in Fig. 12a (the tangential stress increases right from the start of depressurisation). In reality, the stress acting perpendicularly to a crack can increase only after closure of the crack. Another aspect of the model behaviour is that the displacement u of the cavity wall at the maximum and minimum pressures does not vary with the number of cycles. This disagrees with actual rock behaviour; in situ tests in CAES and gas storage pilot plants show that the cavern diameter increases with the number of cycles (Stille et al., 1994; Okuno et al., 2009).

We will next discuss the computational results for the case of a rock mass with lower uniaxial compressive strength (7 MPa). Up to an air pressure of 7 MPa, the response of the model is exactly the same as before (path *OABC*, Fig. 13a). During pressurisation from 5 MPa to 7 MPa (path *BC*), a cracked region develops, inside which the stress state is uniaxial. When the air pressure reaches the uniaxial compressive strength, σ_c, the rock fails in shear (so-called passive shear failure). During further pressurisation, the tangential stress increases with the air pressure, so that the stress state moves along the failure surface (path *CD*). Next to the cavity, a crushed zone develops, which is bounded by an outer cracked zone. The displacement of the cavity wall increases super-linearly with the air pressure (Fig. 13c). As can be seen from the radial distributions of the stresses (Fig. 13b), at the maximum air pressure of the first cycle, the crushed zone extends up to a radius of 6.8 m, while the cracked zone extends up to a radius of 9.5 m.

During the first depressurisation of the cavity, the response is initially elastic (path *DE*); the tangential stress increases by the same amount as the radial stress decreases and becomes the maximum principal stress when the air pressure drops below 10 MPa. At a certain air pressure p^* (point *E*, 3.3 MPa in the present example), the stress state reaches the failure surface (so-called active shear failure). Afterwards, the stress state moves along the failure surface (path *EF*) and a crushed zone with a gradually increasing radius develops around the cavity. The displacement of the cavity wall depends initially linearly (path *DE*, Fig. 13c) and afterwards nonlinearly (path *EF*, Fig. 13c) on the air pressure. At the end of the cycle, the tangential stress is equal to the uniaxial compressive strength of the rock (point *F*). The dashed lines in Fig. 13b show the radial distributions of the stresses after complete depressurisation; the peak of tangential stress at $r = 2.8$ m marks the boundary of the crushed zone. Again, a residual positive displacement can be observed at the end of the first cycle (point *F* in Fig. 13c).

During the next pressurisation, the response is initially elastic (path *FG*, Fig. 13a). When the air pressure increases above the uniaxial compressive strength of the rock, the stress state moves on the failure surface (path *GD*). The stress path during the second depressurisation is the same as in the first cycle (path *DEF*). In all following cycles, the stress state moves along path *FGDEF*. The stress distributions of Fig. 13b remain the same for all cycles. The outer radii of the cracked zone and of the passive shear zone at the maximum air pressure as well as the radius of the active shear zone after every complete depressurisation remain constant over the cycles. The same is also true with respect to the displacement of the

Table 2
Parameter values assumed in the numerical rock-lining interaction analyses performed for the assessment of buckling and fatigue.

Rock mass	Uniaxial compressive strength, σ_c (MPa)	Friction angle, ϕ (°)	Tensile strength, σ_t (MPa)	Dilatancy angle, ψ (°)	Young's modulus, E (GPa)	Poisson's ratio, ν
	≥5	30	0	0	2–20	0.3
Steel lining	Thickness, t (mm)	Internal radius, a (m)	Yield strength, σ_y (MPa)	Young's modulus, E_s (GPa)	Poisson's ratio, ν_s	
	10	2	355	198	0.3	
Initial stress field (homogeneous and isotropic)	Initial stress, σ_0 (MPa)					
	2.5					

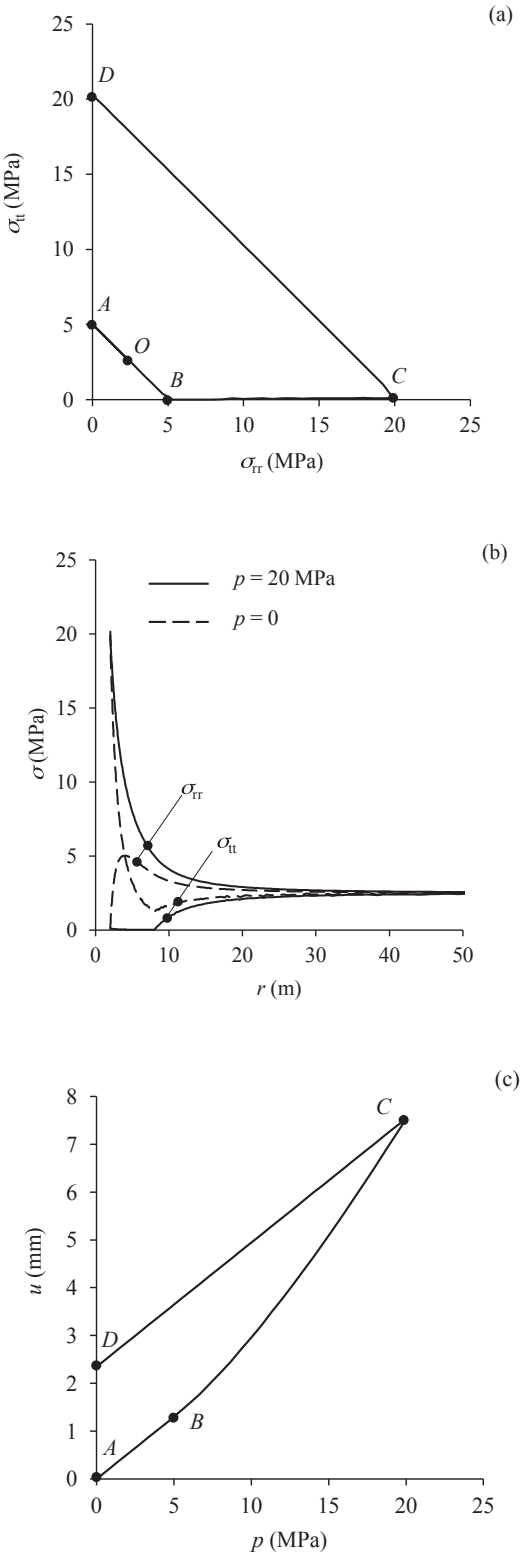

Fig. 12. Numerical results for an unlined cavity and a rock strength $\sigma_c > 20$ MPa: (a) Stress path of the rock at the cavity boundary during excavation of the cavity and cyclical pressurisation; (b) Radial distribution of the radial (σ_{rr}) and tangential (σ_{tt}) stresses at the maximum (solid lines) and minimum (dashed lines) air pressures; (c) Displacement of the cavity boundary as a function of the air pressure p (unlined cavity, cyclical pressure variable between $p_{max} = 20$ MPa and $p_{min} = 0$; $E = 10$ GPa, other parameters as in Table 2).

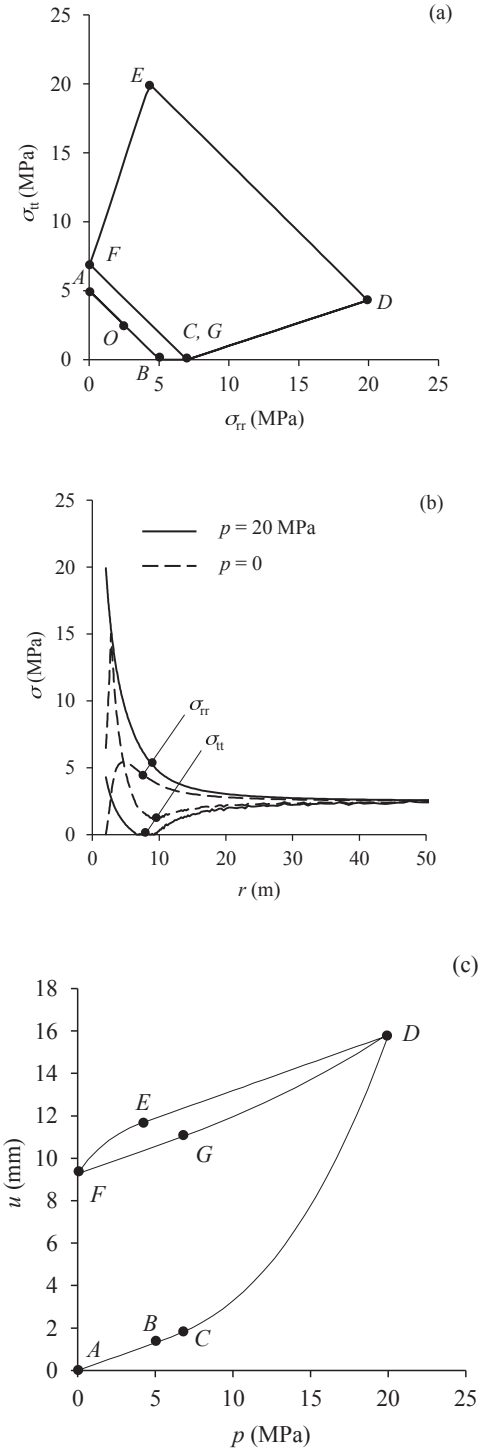

Fig. 13. Numerical results for an unlined cavity and a rock strength $\sigma_c = 7$ MPa: (a) Stress path of the rock at the cavity boundary during excavation of the cavity and cyclical pressurisation; (b) Radial distribution of the radial (σ_{rr}) and tangential (σ_{tt}) stresses at the maximum (solid lines) and minimum (dashed lines) air pressures; (c) Displacement of the cavity boundary as a function of the air pressure p (unlined cavity, cyclical pressure variable between $p_{max} = 20$ MPa and $p_{min} = 0$; $E = 10$ GPa, other parameters as in Table 2).

cavity wall. It increases along path *FGD* during every pressurisation, but decreases along path *DEF* during every depressurisation (see Fig. 13c).

Contrary to the in situ observations, the displacements at the maximum and minimum air pressures (points *D* and *F* in Fig. 13c) do not change with the number of cycles, although the rock experiences failure repeatedly during the cyclical loading. Comparative computations show that this behaviour is also related to the assumption of a zero dilatancy angle. In the case of dilatant behaviour, the displacements at the maximum and minimum air pressures decrease over the cycles. The effect of dilatancy deserves further investigation. Another limitation of the constitutive model is that it does not account for softening behaviour (the failure surfaces do not change with the cycles). In view of the stress path, softening is probably an important factor.

4.4. Rock-lining interaction under cyclical loading

This interaction between the rock and the lining will be discussed for the two sets of geotechnical conditions, considering additionally the constraint imposed by a 10 mm thin steel shell.

Fig. 14 shows the relation between the air pressure p and the pressure p_r acting on the rock (upper diagram) as well as the tangential stress $\sigma_{tt,s}$ and strain $\varepsilon_{tt,s}$ experienced by the steel (lower diagram), assuming that the rock strength is higher than the maximum air pressure ($\sigma_c > 20$ MPa).

At the start of pressurisation (curve *OA*), a small portion of the air pressure p is borne by the lining and the remaining part is transferred to the rock (Fig. 14a). The lining loading ($q = p - p_r$) induces tangential tensile stress $\sigma_{tt,s}$ in the steel (Fig. 14b). At a certain air pressure p_A (point *A*), the steel yields ($\sigma_{tt,s} = \sigma_y$). Afterwards (line *AB*), the air pressure exceeding p_A is transferred to the rock. If the maximum air pressure p_B (point *B*) is too great, then the steel lining fails due to excessive deformation ($\varepsilon_{tt,s} = \varepsilon_{tt,s\ lim}$). This hazard scenario was investigated in the previous section.

During depressurisation (line *BCD*), both the rock pressure p_r and the lining loading q decrease. At a certain air pressure, the lining loading q and the tangential stress in the steel become zero (point *C*). Further depressurisation (line *CD*) causes compression of the lining. If the compression load q is too large, the steel lining fails by buckling. The compression load q and the subsequent risk of buckling are the highest after complete depressurisation (point *D*) and increase with increasing maximum air pressure. Buckling is analysed in Section 4.5.

During the first depressurisation and during the next cycles, the relationship between the air pressure p and the pressure p_r acting on the rock is linear and it does not vary under loading and reloading (line *DCB*, Fig. 14a). The variations in the tangential stress $\sigma_{tt,s}$ and strain $\varepsilon_{tt,s}$ during the cycles are also linear and given by the line *DCB* in Fig. 14b. The maximum compression load ($q = 0.68$ MPa for $p = 0$) and the stress range experienced by the steel in a single cycle $\Delta\sigma_{tt,s}$ ($\Delta\sigma_{tt,s} = 504$ MPa) do not increase with the number of cycles. These aspects of the rock-lining interaction are due to the behaviour of the rock, which was discussed in the previous section (Section 4.3); the stress and strain in a rock mass having $\sigma_c > 20$ MPa vary elastically during the first depressurisation and during the next cycles (see Fig. 12).

The repeated loading and unloading of the lining induce the risk of fatigue failure of the steel. Decisive factors in this respect are the number of cycles and the stress range in a single cycle $\Delta\sigma_{tt,s}$, and the latter increases with the maximum air pressure and with decreasing minimum air pressure. It should be noted that the latter will be atmospheric only for the performance of maintenance work. During normal CAES operation, the minimum air pressure amounts

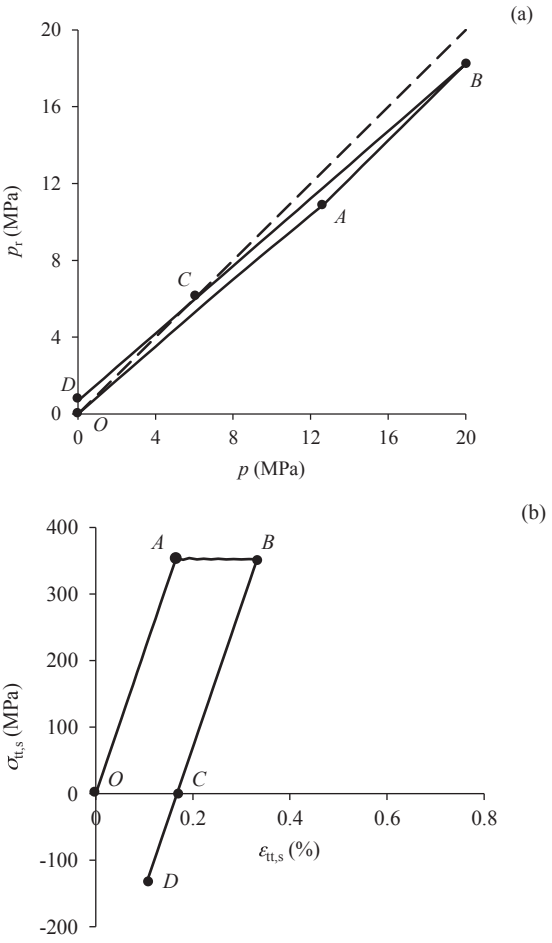

Fig. 14. Numerical results for a lined cavity and a rock strength $\sigma_c > 20$ MPa: (a) Pressure acting on the rock at the cavity boundary p_r as a function of the air pressure p; (b) Stress ($\sigma_{tt,s}$) and strain ($\varepsilon_{tt,s}$) of the steel during cyclical pressurisation (cyclical pressure variation between $p_{max} = 20$ MPa and $p_{min} = 0$; $\sigma_c > 20$ MPa, $E = 10$ GPa, other parameters as in Table 2).

to 2–4 MPa (Johansson, 2003). This will be taken into account in the fatigue assessment (Section 4.6).

The second example (Fig. 15) assumes that the rock strength is lower than the maximum air pressure ($\sigma_c = 7$ MPa). Figs. 15b and 14b clearly show that the steel experiences a high tangential strain in this case. This is due to the passive shear failure of the rock, which reduces the stiffness of the rock and occurs when the pressure p_r at the rock-lining interface exceeds the uniaxial compressive strength of the rock. The relationship between the air pressure p and the pressure p_r is also slightly nonlinear during the first depressurisation (line *BCD*, Fig. 15a). This is due to the active shear failure (see the previous section and Fig. 13). The failure-induced decrease in rock stiffness also leads to a higher compression load at the end of the first depressurisation ($q = 0.89$ MPa versus 0.68 MPa for $p = 0$).

Due to the repeated shear failures occurring in loading and unloading (Fig. 13), the relationships between the air pressure p and the pressure p_r acting on the rock (lines *DEB* and *BCD* during loading and reloading, respectively) are also slightly nonlinear in the second and subsequent cycles. The tangential stress $\sigma_{tt,s}$ and strain $\varepsilon_{tt,s}$ in the steel vary elastically during cyclical loading (line *DB* in Fig. 15b); the minimum and maximum strains $\varepsilon_{tt,s}$ and the stress range $\Delta\sigma_{tt,s}$ remain constant over the cycles. It should be noted that comparative analyses, which are not presented here, show that if

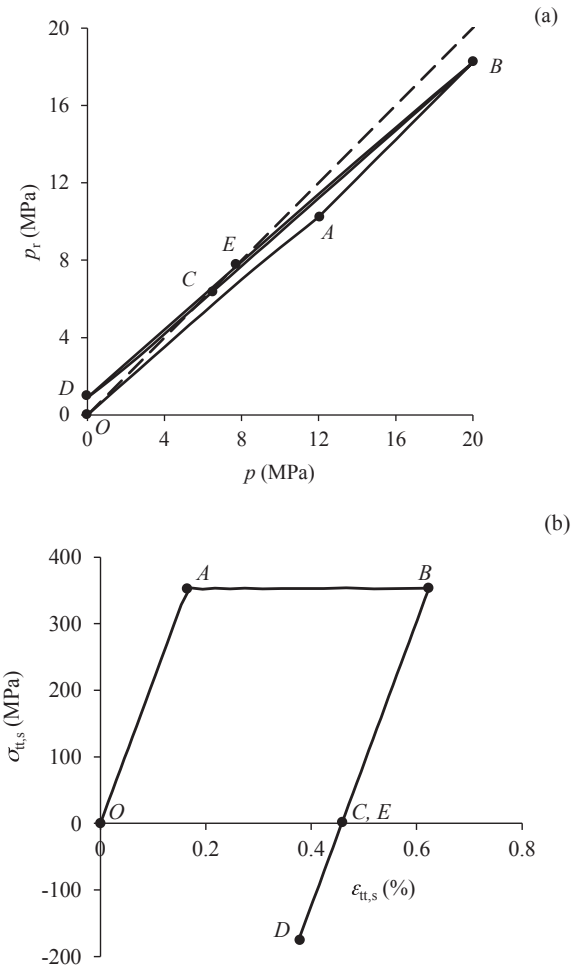

Fig. 15. Numerical results for a lined cavity and a rock strength $\sigma_c = 7$ MPa: (a) Pressure acting on the rock at the cavity boundary p_r as a function of the air pressure p; (b) Stress ($\sigma_{tt,s}$) and strain ($\varepsilon_{tt,s}$) of the steel during cyclical pressurisation (cyclical pressure variation between $p_{max} = 20$ MPa and $p_{min} = 0$, $\sigma_c > 20$ MPa, $E = 10$ GPa, other parameters as in Table 2).

the rock behaviour is dilatant, then the compression load q increases and the minimum and maximum deformations $\varepsilon_{tt,s}$ decrease over the cycles. As mentioned in last section, the effect of dilatancy is not yet understood and deserves further investigation.

4.5. Buckling failure

4.5.1. Buckling analysis

The critical buckling load q_{cr} was determined (Trombetta, 2015) by nonlinear buckling analyses based on the model shown in Fig. 16. The rock was handled by introducing discrete normal springs with nonlinear behaviour, allowing for rock-lining separation (Fig. 16b). The springs provide a reaction only for outward displacements of the ring, i.e. they can bear only compressive forces. Their stiffness k_{sp} was taken equal to

$$k_{sp} = Ebd/[(1-\nu)a] \quad (1)$$

where E and ν are the elasticity constants of the rock; d is the spacing of the springs (Fig. 16a, here $d = 0.09$ m); and b and a denote the width (1 m) and the radius (2 m) of the lining. The latter was modelled by elastic beam elements having a cross-section of

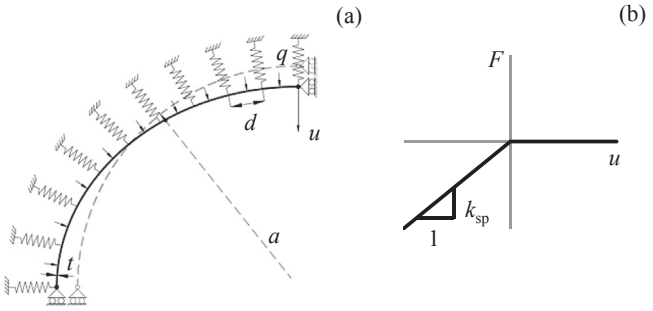

Fig. 16. Computational model of the buckling analysis (after Trombetta, 2015).

1 m × 0.01 m and, due to the plane strain conditions, a Young's modulus, which is written as

$$E_b = E_s \Big/ \left(1-\nu_s^2\right) \quad (2)$$

A global oval-shaped imperfection was assumed (Fig. 16a), corresponding to the first buckling mode of the linear buckling analysis. A uniform pressure q was assumed to act over the entire lining.

The analyses were performed (Trombetta, 2015) using the commercial code Abaqus (Dassault Systèmes, 2010) based upon the modified Riks method. Fig. 17 shows the pressure-deflection curves obtained for various values of Young's moduli of the rock. The maxima of the curves correspond to the critical buckling pressures q_{cr}. As expected, the buckling pressure q_{cr} decreases with a decreasing Young's modulus of the rock. The solid line in Fig. 18 shows the buckling pressure q_{cr} as a function of the Young's modulus of the rock. For comparison, the diagram includes two analytical solutions: the one of Levy (1884), derived for unconfined rings, and the one of Glock (1977), derived for rings embedded in a rigid medium. With a decreasing Young's modulus E, the buckling pressure tends asymptotically to a minimum value, which corresponds to the limit case of an unconfined ring and is very close to the solution of Levy (1884). With an increasing modulus E, the buckling pressure tends asymptotically to a maximum value, which corresponds to the limit case of rigid confinement and is close to the solution of Glock (1977). Note that for the typical values of the Young's modulus E (higher than 1 GPa for rocks), the buckling pressure q_{cr} does not depend significantly on E and is very close to the buckling pressure of a ring embedded in a rigid medium.

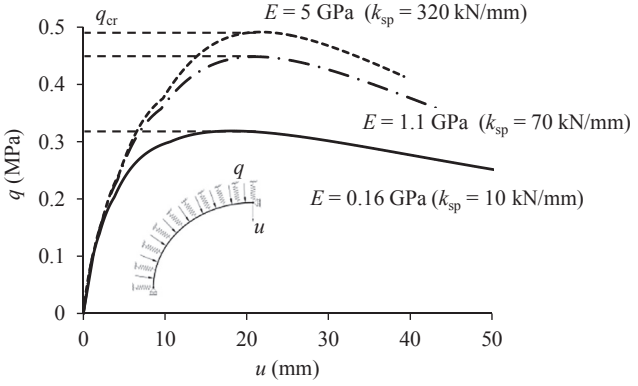

Fig. 17. Relationship between pressure q and displacement u of a control point according to the buckling analysis ($a = 2$ m, $t = 10$ mm, $E_s = 198$ MPa, $\nu_s = 0.3$, $\nu = 0.3$) (after Trombetta, 2015).

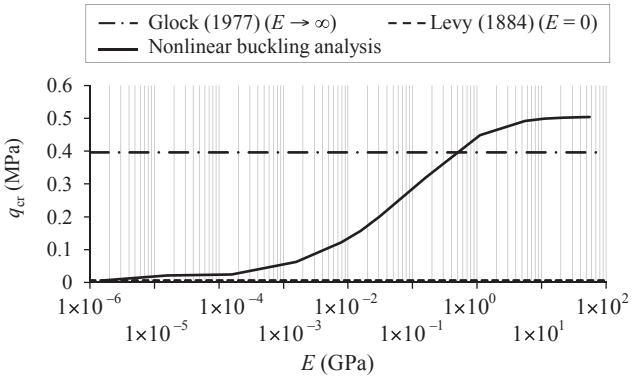

Fig. 18. Buckling pressure q_{cr} as a function of the Young's modulus of the rock ($a = 2$ m, $t = 10$ mm, $E_s = 198$ GPa, $\nu_s = 0.3$, $\nu = 0.3$) (after Trombetta, 2015).

4.5.2. Assessment

For the assessment of safety against buckling, we compare the buckling load determined above (dashed line in Fig. 19) with the actual load (solid lines in Fig. 19). The latter takes its maximum value at the end of every depressurisation and increases with a decreasing strength σ_c and Young's modulus E of the rock mass. In Fig. 19, it can be observed that the actual load exceeds the critical load q_{cr}, if the Young's modulus of the rock is lower than 12–15 GPa (depending on the rock strength).

As explained in Section 4.4, the load developing upon the lining after complete depressurisation increases with the maximum operational air pressure. Fig. 20 shows (for the same geotechnical conditions as Fig. 19) the maximum operational pressure p_b that results in an actual load equal to the critical load q_{cr}. For every parameter set, the pressure p_b was determined by performing a series of numerical stress analyses (with the model of Section 4.2) for different, closely spaced values of the maximum air pressure (the minimum air pressure was taken equal to zero). The numerical analyses provided the relationship between the maximum air pressure and the loading q at zero air pressure. The critical pressure p_b, i.e. the one corresponding to the critical load q_r, was determined by linear interpolation.

The results of Fig. 20 can be used to assess the safety against buckling for a given maximum air pressure (or to determine a safe maximum operational pressure). In soft rock masses (2 GPa < E < 5 GPa), the maximum air pressure should not exceed

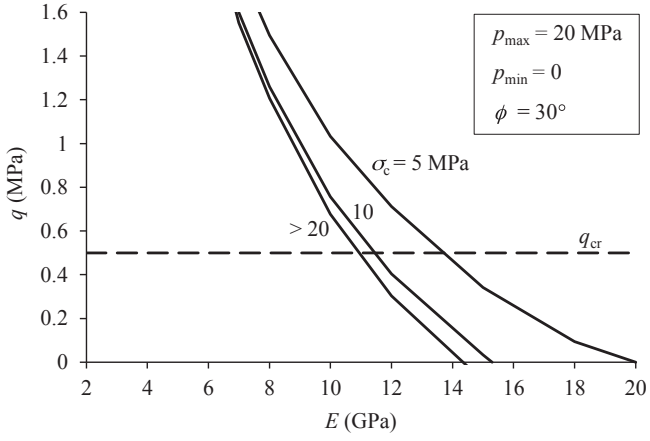

Fig. 19. Compression load q on the lining after complete depressurisation of the cavity ($p_{min} = 0$) as a function of the Young's modulus E of the rock mass ($p_{max} = 20$ MPa, other parameters as in Table 2).

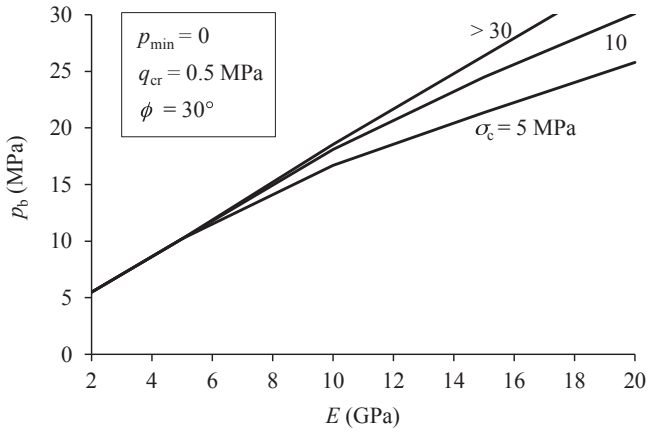

Fig. 20. Pressure p_b at which the compression load q at $p_{min} = 0$ is equal to the buckling load q_{cr} as a function of the Young's modulus E of the rock mass ($q_{cr} = 0.5$ MPa, other parameters as in Table 2).

10 MPa (e.g. $p = 5$ MPa for $E = 2.5$ GPa). This value is lower than the critical air pressure that was determined from the criterion of steel strain (14 MPa for 100 m depth of cover, $\sigma_c = 5$ MPa and $E = 2.5$ GPa, see Fig. 10). Consequently, safety against buckling is the decisive criterion for soft rock masses.

4.6. Fatigue failure

The safety against fatigue failure in the steel lining depends, in general, on the number of loading cycles, on the stress range $\Delta\sigma_{tt,s}$ in a single cycle and on the type of welding joints. As suggested in various technical specifications, the critical stress range $\Delta\sigma_{scr}$ can be expressed as a function of the weld type and the number of cycles. For example, according to BS EN 13445–3 (2009), the critical stress range $\Delta\sigma_{scr}$ for 10,000 cycles is equal to 526 MPa for joints of very good quality (joint class 90) and to 369 MPa for joints of medium quality (joint class 70).

Fig. 21 shows the actual stress range $\Delta\sigma_{tt,s}$ (solid lines) of the lining as a function of the strength σ_c and the Young's modulus E of the rock mass for CAES cavities under a cyclical air pressure variation of 2–20 MPa. The diagram was computed with the model from Section 4.2, taking a single loading–unloading cycle. The stress range $\Delta\sigma_{tt,s}$ increases with decreasing rock stiffness and strength. The effect of the strength σ_c is not, however, significant. For comparison, the diagram also shows the critical stress range $\Delta\sigma_{scr}$ for two joint qualities (dashed line). In CAES cavities with a

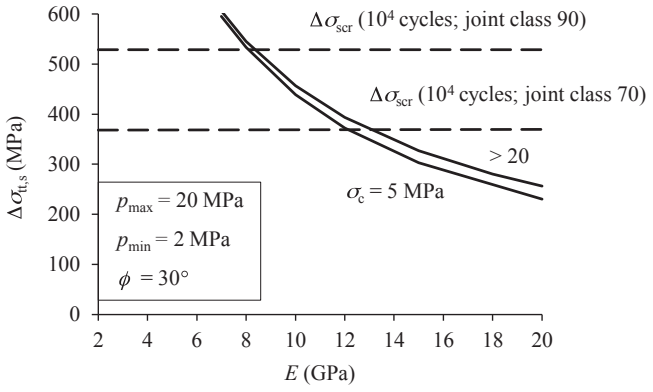

Fig. 21. Stress range in the steel $\Delta\sigma_{tt,s}$ during cyclical pressurisation as a function of the Young's modulus E of the rock mass ($p_{max} = 20$ MPa, $p_{min} = 2$ MPa, other parameters as in Table 2).

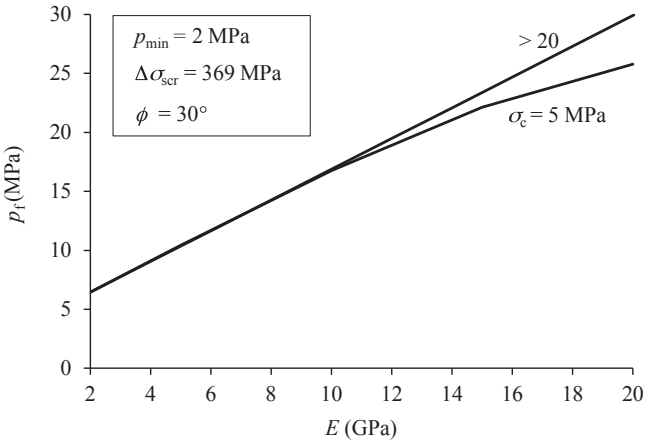

Fig. 22. Pressure p_f at which the stress range in the steel $\Delta\sigma_{tt,s}$ is equal to the critical stress range $\Delta\sigma_{scr}$ for the fatigue as a function of the Young's modulus E of the rock mass (p_{min} = 2 MPa, $\Delta\sigma_{scr}$ = 369 MPa, other parameters as in Table 2).

maximum operating pressure of 20 MPa, the actual stress range of the lining exceeds the critical stress range $\Delta\sigma_{scr}$, if the Young's modulus of the rock mass is lower than 8–13 GPa (depending on the weld type).

The actual stress range experienced by the steel during cyclical loading increases with the maximum operational air pressure (see Section 4.4). Fig. 22 shows (for a minimum air pressure of 2 MPa and the same geotechnical conditions as shown in Fig. 21) the maximum operational pressure p_f that results in a stress range of 369 MPa, which is critical for joint class 70 and 10,000 loading–unloading cycles. The diagram, which was computed analogously in Fig. 20, shows that the maximum air pressure should be lower than 10 MPa for 2 GPa < E < 5 GPa, which means that for CAES cavities in soft rocks, fatigue failure is as relevant as buckling.

5. Plug stability

In the section, we consider the example of an 80 m deep CAES tunnel of 4 m diameter located above the water table and accessed by a service tunnel of equal diameter (Fig. 23a). Plugs of different dimensions (L_p, t_p) are studied.

We performed numerical stress analyses (based on the axisymmetric model in Fig. 23b) in order to estimate the plug loading that would cause collapse of the rock mass. The numerical model does not take into account the tunnel linings or the manhole in the plug. The rock mass is modelled as a continuous linear elastic-perfectly plastic, no-tension material, obeying the Mohr–Coulomb yield criterion. A weak rock mass was considered (parameters are given in the caption of Fig. 24). The concrete plug is taken as a linearly elastic (E_{cr} = 40 GPa, ν_{cr} = 0.3), practically rigid material. Practically rigid–plastic interface elements (interface shear stiffness K_{sI} = 500 GPa/m, interface normal stiffness

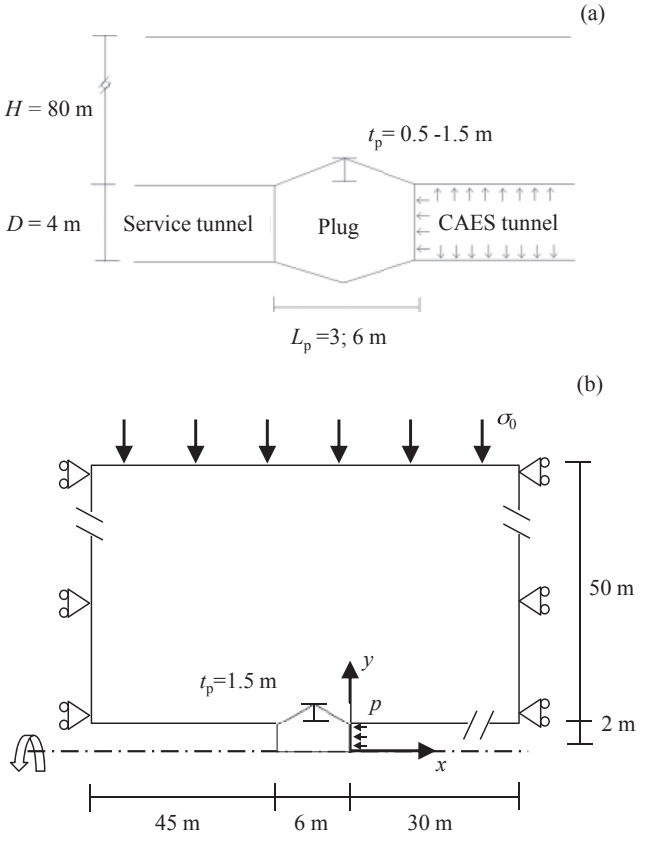

Fig. 23. (a) Geometry of the investigated plugs; (b) Computational domains and boundary conditions adopted in the numerical stress analyses of a specific plug (L_p = 6 m, t_p = 1.5 m).

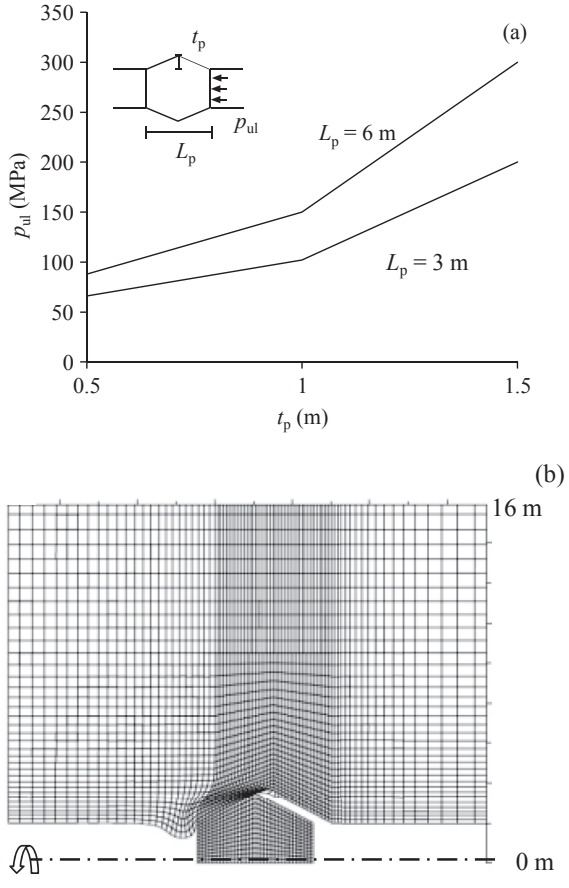

Fig. 24. (a) Ultimate pressure as a function of the dimensions of the plug; (b) Deformed calculation grid for a specific plug (L_p = 6 m, t_p = 1.5 m) at the ultimate pressure p_{ul} = 300 MPa (rock mass with σ_0 = 2 MPa, ϕ = 30°, σ_c = 8 MPa, σ_t = 0, ψ = 0°, E = 5 GPa, ν = 0.3).

$K_{nl} = 500$ GPa/m) with purely frictional strength ($\phi_l = 25°$) are used to model the contact between the plug and the rock mass.

The analysis consists of the following steps: (1) initialization of the in situ stress field, assuming a uniform and isotropic stress distribution ($\sigma_0 = \gamma H = 2$ MPa); (2) simulation of the excavation by deleting the grid elements inside the CAES tunnel, inside the service tunnel and inside the plug in a single step without the application of any support; (3) simulation of plug installation by reactivating the grid elements inside the plug; and (4) application of an increasing internal pressure on the plug (no cyclical loading). We applied an internal pressure only on the plug (Fig. 23b) because the first analyses showed that the limit load of the rock mass in the plug area is higher than that of the rock mass around the CAES tunnel. In order to estimate the stability of the rock mass subjected to plug loading, we evaluate the relationship between the displacement of a control point (on the wall of the service tunnel) and the pressure applied on the plug. The critical pressure is taken equal to the pressure at the last equilibrated solution.

Fig. 24a shows the critical pressure as a function of the conicity t_p and the length L_p of the plug. The critical pressure increases with increasing plug length and conicity. For typical operational pressures of up to 20 MPa, 3–6 m long plugs with a conicity of 0.5–1.5 m are not critical for the stability of the rock mass. Nevertheless, a small conicity (e.g. $t_p < 1.5$ m) is not recommended, because the rock mass close to the tunnel may have been disturbed by the excavation. The safety factor against failure of the concrete is decisive for selecting the length of the plug.

Fig. 24b shows the deformed calculation grid at the last equilibrated solution. As expected, the plug separates from the rock mass along the interface on the side of the CAES tunnel. This is an important aspect to be considered in lining design (Okuno et al., 2009). The structural detailing of the lining must be such that it is able to bridge the gap without becoming damaged and, particularly, without losing its tightness.

6. Conclusions

In shallow CAES cavities, uplift failure of the overlying rock mass is an important hazard scenario considering the air pressures needed for efficient energy storage ($p = 10–30$ MPa). For a given maximum operational pressure, safety against uplift depends significantly on rock strength, depth of cover, horizontal stress and cavity type (tunnel or shaft). The critical overburden for 4 m diameter CAES tunnels with the maximum air pressure of 20 MPa amounts to 60–120 m, depending on the geotechnical conditions. CAES shafts can be constructed in smaller depths (30–50 m).

The safety of the rock mass against uplift failure is a necessary but not a sufficient condition for the feasibility of a CAES cavity. A high maximum air pressure may cause tensile, fatigue or buckling failure of the steel lining. Safety against these failure types increases with rock stiffness, but does not depend on the type of cavity (tunnel or shaft). The computational results lead to the conclusion that safety against buckling or fatigue failure is the decisive factor for the maximum air pressure if the rock is soft and the storage utility is not too shallow. At a depth of 100 m, which would not be problematic with respect to uplift safety for CAES facilities under 20 MPa pressure in tunnels and shafts of 4 m diameter, safety against fatigue or buckling limits the operational air pressures to a maximum of 10 MPa, if the rock is softer than 5 GPa.

The stability of the rock mass under the plug loading is another hazard scenario. It was investigated here assuming specific geotechnical conditions and plug geometries similar to those applied in previous studies (plug length 6 m, conicity 0.5–1.5 m). The computational results indicate that rock failure around the plug is not a relevant design factor.

The present paper analysed CAES cavities above the water table. Drainage measures would be essential underneath the water table in order to avoid buckling of the steel lining in the depressurisation stage; thin, economically viable steel shells may buckle even under a low hydrostatic pressure of about 5 bars in the example of Section 4.5.1 (1 bar $= 1 \times 10^5$ Pa). Groundwater drainage over the entire lifetime of the system may be environmentally unacceptable. Basically, one might switch the drainage system on and off during the depressurisation and pressurisation phases, respectively. Intermittent operation of the drainage system, however, would reduce the overall reliability of the system and raise questions over the response time of the ground to drainage in relation to the frequency of cycles. These issues may significantly affect the feasibility of lined CAES systems and they deserve further investigations.

The computational results also illustrate some limitations of the widely used constitutive models (e.g. their failure to map the closing of open cracks), which may be very important for studying the rock-lining interaction during cyclical loading. In view of the inherent model and parameter uncertainties as well as the lack of experience with this type of underground opening, properly monitored field tests in scaled models will be indispensable for evaluating the feasibility of underground CAES facilities under the specific geotechnical conditions of a project site.

Conflict of interest

The authors wish to confirm that there are no known conflicts of interest associated with this publication and there has been no significant financial support for this work that could have influenced its outcome.

Acknowledgements

The authors wish to thank Herrenknecht AG, Germany, which has supported this research project. Further thanks are due to Dr. Yasunori Ootsuka (OYO Corporation, Japan) for the valuable discussions and suggestions.

Notation

a	internal radius of the steel lining
b	width of the lining (Eq. (1))
D	diameter
d	spacing of the springs (Fig. 16a)
E	Young's modulus of the rock mass
E_s	Young's modulus of the steel
E_{cr}	Young's modulus of the concrete plug
F	spring reaction (Fig. 16b)
H	overburden
K_0	coefficient of lateral stress at rest
K_{sl}	shear stiffness of the interface elements
K_{nl}	normal stiffness of the interface elements
k_{sp}	stiffness of the springs (Fig. 16b)
L	height of the shaft
L_p	length of the plug (Fig. 23a)
p	air pressure
p_b	critical air pressure for buckling
p_c	critical air pressure for cracking until surface
p_f	critical air pressure for fatigue failure
p_r	pressure on the rock (Fig. 11b)
p_u	ultimate air pressure
p_{max}	maximum air pressure
p_{min}	minimum air pressure

p^*	air pressure at which active shear failure of the rock occurs during depressurisation
q	lining load (Fig. 16a)
q_{cr}	critical buckling load
r	radial coordinate
t	thickness of the steel lining
t_p	conicity of the plug (Fig. 23a)
u	radial displacement
x	horizontal coordinate
y	vertical coordinate

Greek symbols

γ	unit weight of the rock mass
$\Delta\sigma_{tt,s}$	stress range in the steel lining
$\Delta\sigma_{scr}$	critical stress range for fatigue failure of the steel
ε_{tt}	tangential deformation of the rock mass
$\varepsilon_{tt\ lim}$	limit tangential deformation of the rock mass
$\varepsilon_{tt,s}$	tangential deformation of the lining
$\varepsilon_{tt,s\ lim}$	limit tangential deformation of the steel lining
ν	Poisson's ratio of the rock mass
ν_s	Poisson's ratio of the steel
ν_{cr}	Poisson's ratio of the concrete plug
σ	normal stress
σ_c	uniaxial compressive strength of the rock mass
σ_t	tensile strength of the rock mass
σ_y	yield strength of the steel
σ_{rr}	radial stress in the rock mass
σ_{tt}	tangential stress in the rock mass
$\sigma_{tt,s}$	tangential stress in the lining
σ_{xx}	horizontal stress
σ_{yy}	vertical stress
σ_{xx0}	horizontal initial stress
σ_{yy0}	vertical initial stress
σ_0	initial homogeneous isotropic stress
ϕ	friction angle of the rock mass
ϕ_l	Friction angle of the plug–rock interface
ψ	dilatancy angle of the rock mass

References

Auld FA. Design of underground plugs. International Journal of Mining Engineering 1983;1(3):189–228.

Brandshaug T, Christianson M, Damjanac B. Technical review of the lined rock caverns (LRC) concept and design methodology: mechanical response of rock mass. Minneapolis, Minnesota: Itasca Consulting Group, Inc; 2001.

BS EN 13445–3. Unfired pressure vessels – part 3: design. BSI British Standards 2009.

Crotogino F, Mohmeyer KU, Scharf R. Huntroft CAES: more than 20 years of successful operation. In: Solution Mining Research Institute (SMRI) Spring 2001 Meeting. Orlando, Florida, USA; 2001. p. 15–8.

Dassault Systèmes. Abaqus: theory manual. Ver. 6.10. Providence, RI, USA: Dassault Systèmes Simulia Corp.; 2010.

Damjanac B, Carranza-Torres C, Dexter R. Technical review of the lined rock caverns (LRC) concept and design methodology: steel liner response. Minneapolis, Minnesota: Itasca Consulting Group, Inc; 2002.

Gardner J, Haynes T. Overview of compressed air energy storage. Boise, ID, USA: Boise State University; 2007.

Glock D. Post-critical behavior of a rigidly encased circular pipe subject to external water pressure and temperature rise. Der Stahlbau 1977;46(7):212–7.

Hökmark H. Numerical study of the performance of tunnel plugs. Engineering Geology 1998;49(3):327–35.

Ilyushin VF. Design of concrete plugs in temporary underground hydraulic structures. Gidrotekhnicheskoe Stroitel'stvo 1988;(6):16–8.

Itasca Consulting Group, Inc. FLAC: user's manual. Ver. 4.0. Minneapolis, Minnesota USA: Itasca Consulting Group, Inc.; 2001.

Johansson J. High pressure storage of gas in lined rock caverns – cavern wall design principles. Licentiate Thesis. Stockholm, Sweden: Division of Soil & Rock Mechanics, Royal Institute of Technology; 2003.

Kim HM, Park D, Ryu DW, Song WK. Parametric sensitivity analysis of ground uplift above pressurized underground rock caverns. Engineering Geology 2012;135–136:60–5.

Kovári K. Basic consideration on storage of compressed natural gas in rock chambers. Rock Mechanics and Rock Engineering 1993;26(1):1–27.

Ladanyi B. Expansion of cavities in brittle media. International Journal of Rock Mechanics and Mining Sciences & Geomechanics Abstracts 1967;4(3):301–28.

Levy M. Memoire sur un nouveau cas integrable du problem de l'elastique et l'une de ses applications. Journal de Mathématiques Pures et Appliquées, Lioville 1884;10(3):5–42 (in French).

Mansson L, Marion P. The LRC concept and the demonstration plant in Sweden – a new approach to commercial gas storage. In: Proceedings of the IGU World Gas Conference 2003. Tokyo; 2003.

Okuno T, Wakabayashi N, Niimi K, Kurihara Y, Iwano M. Advanced natural gas storage system and verification tests of lined rock cavern – ANGAS project in Japan. International Journal of the JCRM 2009;5(2):95–102.

Park BK, Lee HK, Jeon S. Numerical study on mechanical and hydraulic behaviour of concrete plug in an underground cavern. In: Proceedings of the 10th IACMAG. Computer Methods and Advances in Geomechanics. Tucson, Arizona, USA; 2001. p. 1719–24.

Pedretti A, Vietti D, Bazzi Pedrazzini M, Neuenschwander M. Reuse of abandoned underground structures – the compressed air energy storage test plant in Switzerland. In: Anagnostou G, Ehrbar H, editors. World Tunnel Congress 2013, Geneva. London: Taylor & Francis Group; 2013. p. 7.

Perazzelli P, Anagnostou G, Amberg J. Uplift analysis for CAES tunnels. In: The 14th International Conference of the International Association for Computer Methods and Advances in Geomechanics. Kyoto: CRC Press; 2014. p. 1691–6.

Satapathy S, Bless S. Cavity expansion analysis of brittle materials. Technical Report. Austin: Institute for Advanced Technology, The University of Texas at Austin; 1995.

Sofregaz US Inc., LRC. Commercial potential of natural gas storage in lined rock caverns (LRC). Houston, Texas, USA: Sofregaz US Inc; 1999.

Song WK, Ryu DW. Stability analysis of concrete plugs in a pilot cavern for compressed air energy storage. In: Qian QH, Zhou YX, editors. Proceedings of the 12th ISRM International Congress on Rock Mechanics. Harmonising Rock Engineering and the Environment. Rotterdam: A.A. Balkema; 2012. p. 676–7.

Stille H, Johansson J, Sturk R. High pressure storage of gas in lined shallow rock caverns – results from field tests. In: Proceedings of the SPE/ISRM Conference. Rotterdam: A.A. Balkema; 1994. p. 689–96.

Trombetta L. Geomechanical and structural aspects in the design of tunnels for CAES (compressed air energy storage). MS Thesis. ETH Zurich: Università degli Studi "Roma Tre"; 2015.

Tunsakul J, Jongpradist P, Soparat P, Kongkitkul W, Nanakorn P. Analysis of fracture propagation in a rock mass surrounding a tunnel under high internal pressure by the element-free Galerkin method. Computers and Geotechnics 2014;55:78–90.

Dr. Paolo Perazzelli graduated in environmental engineering from University of Rome "Sapienza" in 2007. From 2007 to 2010 he was a research associate in the Department of Geotechnical Engineering of "Sapienza" University. In 2011 he received his Ph.D. degree with a thesis on tunnelling in soft soils. Subsequently, he transferred to industry and worked as tunnelling engineer in Astaldi. Since 2012 he is postdoctoral research fellow in the Tunnelling Group of the ETH Zurich where he is involved in research works dealing with deformation and stability problems of underground structures in soil and rock.

Contact information: ETH Zurich, Stefano Franscini Platz 5, 8093 Zurich, Switzerland.
Tel: +41-(0)44 6330729
E-mail: paolo.perazzelli@igt.baug.ethz.ch

Dr. G. Anagnostou graduated in civil engineering from the University of Karlsruhe in 1983. From 1983 to 1993 he was a research associate at the Rock Mechanics and Tunnelling Group of the ETH Zurich. In 1991 he received his Ph.D. degree with a thesis on tunnelling in swelling rock. Subsequently, he transferred to industry and worked as a consulting engineer in Zurich and Athens. He was involved in several tunnelling projects in Switzerland and abroad. In 2003 he was appointed Professor of Tunnelling at ETH Zurich. His research focuses on deformation and stability problems of underground structures in soil and rock.

Contact information: ETH Zurich, Stefano Franscini Platz 5, 8093 Zurich, Switzerland.
Tel: +41-(0)44 6333180
E-mail: georg.anagnostou@igt.baug.ethz.ch